Han et al. *NPG Asia Materials* (2022) 14:28
https://doi.org/10.1038/s41427-022-00377-5

NPG Asia Materials

ARTICLE Open Access

Precise orientation control of a liquid crystal organic semiconductor via anisotropic surface treatment

Moon Jong Han[1,2], Dayan Wei[3], Hee Seong Yun[4], Seong-hun Lee[5], Hyungju Ahn[6], David M. Walba[3], Tae Joo Shin[5,7] and Dong Ki Yoon[1,4,8]

Abstract

We report a three-dimensional (3D) molecular orientation control of a liquid crystal organic semiconductor (LC-OSC) based on the long-range ordering characteristic of an LC material. To this end, a synthetic LC-OSC molecule, MeOPh-BTBT-C8, with a fluidic nematic (N) phase that is essential for alignment control over a large area and a smectic E (SmE) phase showing high ordering, was prepared. A simple flipping of a sandwich cell made of the LC-OSC material between the top and bottom substrates that have uniaxial–planar degenerated alignment as well as crossed rubbing directions responds to the given surface anchoring condition and temperature gradient. Optical observation of the alignment-controlled LC-OSC was carried out by polarized optical microscopy (POM), and the corresponding charge carrier mobility was also measured by fabricating organic field-effect transistors (OFETs). Our platform offers a facile approach for multidirectional and multifunctional organic electronic devices using the stimulus–response characteristics of LC materials.

Introduction

The Internet of Things (IoT) has developed rapidly with progressively concise and smart forms. These remarkable advances derive from four systems: information collection, transmission, storage, and analysis. To place the IoT in a feasible context, an investigation of these basic elements is necessary. One of the essential elements is a flexible and sometimes biocompatible organic field-effect transistor (OFET), which enables multianalyte sensing with a subsequent decision due to rapid and accurate judgment. For example, an OFET can be used as an indispensable and functional electronic element that works well in data assortment[1–5] and information storage[6–8]. However, for now, the electrical properties of OFETs are relatively low compared to those of conventional inorganic material-based FETs, which are obstacles for practical applications[9–11]. Therefore, an organic semiconductor (OSC) should be newly synthesized, and the fine control of OSCs is also necessary to maximize the performance.

Generally, both the ordering and orientation of OSCs should be finely controlled because electrical properties are directly affected by the intra- and intermolecular arrangement of crystalline structures[12–14]. Therefore, the long-range ordered packing of molecules is critical to minimize domain boundaries as well as defect generation while ensuring good in-plane π–π stacking and the elimination of undesired charge scattering or trapping[15]. Single organic crystals have been fabricated based on physical vapor deposition and are capable of meeting the high mobility requirements of electronics. However, it remains challenging to optimize the thickness and crystal orientation of single crystals[16–19]. To address this challenge, various solution-processable methods have been suggested to generate highly ordered and oriented structures[20,21]. However, it has been challenging to

---

Correspondence: Tae Joo Shin (tjshin@unist.ac.kr) or Dong Ki Yoon (nandk@kaist.ac.kr)
[1]Graduate School of Nanoscience and Technology, Korea Advanced Institute of Science and Technology (KAIST), Daejeon 34141, Republic of Korea
[2]School of Materials Science and Engineering, Georgia Institute of Technology, Atlanta, GA 30332, USA
Full list of author information is available at the end of the article

accurately control the evaporation of solvents, resulting in disorder with unexpected grain boundaries and phase segregation, which deteriorates device performance and reliability[22,23]. Nevertheless, controlling the solvent evaporation for highly oriented molecular configurations through solution processes, including meniscus-guided deposition and off-center spin-coating addition, has been realized to improve molecular ordering by post-thermal annealing treatments[15,24,25]. However, it is difficult to modulate the molecular orientation after solvent evaporation through post-treatment because of the inherent limitations of solution-processable systems.

To overcome the obstacles mentioned above, solvent-free OSC platform systems using liquid crystal (LC) characteristics such as long-range ordering, highly oriented properties, and stimulus response to external fields have been suggested, which can be distinguished from polymeric OSCs[26,27]. However, there are still many subjects to be explored for LC-OSCs in OFETs to take advantage of inherent LC properties, including precisely tuning molecular orientation reversibly and self-healing behavior[28–30], which are also essential in other applications[31–35]. The basic and simplest LC phase, the nematic (N) phase having a sole orientational order, easily induces highly oriented structures on nanogrooves over a large area, which is why the N phase has been widely used in display applications[36–38]. For a smectic (Sm) phase having layers, it is difficult to allow the formation of uniaxial planar-oriented LC structures with conventional alignment methods. Indeed, the highly ordered solid-like SmE phase is well known to not easily realize uniaxial planar alignment, although this phase guarantees high charge carrier mobility at the crystal (Cr) phase[38–40].

Here, we demonstrate the reversible and tunable orientation control of an LC-OSC by flipping a sandwich cell made of a rubbed alignment layer, in which self-healing behavior can be found to show a well-oriented domain. The resultant LC-OSC film exhibits highly ordered and oriented structures and orientation-controllable properties by flipping, which directly provides reversible and tunable optical/electrical properties, as measured by polarized optical microscopy (POM) and organic field-effect transistors. We believe this work can suggest a way to fabricate multidirectional electronic devices facilitated by inherent LC characteristics, modulating optoelectronic signals depending on the subjective molecular orientation by various stimuli.

Materials and methods

Materials and fabrication of the orientation-controllable platform

MeOPh-BTBT-C8 was synthesized following a previous study[38]. For the orientation-controllable platform, the ITO and bare glass substrates were cleaned using acetone and ethanol and deionized water every 15 min. The substrates were spin-coated with planar (PIA-5550-02A, JNC) and vertical anchoring polyimide (AL60702, JSR) followed by thermal annealing treatment at 200 °C for 2 h. To generate the nanogrooves on the substrates, they were treated using the rubbing process by a rubbing machine (RMS-50-M, Namil Optics). For the top substrates of the OFET, Au (40 nm)/Ti (5 nm) electrodes were thermally deposited through a metal shadow mask. Additionally, to induce low contact resistance, self-assembled monolayers (SAMs) were fabricated by spin coating a pentafluorobenzenethiol (PFBT, Sigma–Aldrich): ethanol solution (0.1 wt%) followed by thermal annealing at 120 °C for 1 h. A uniform cell gap was realized by the silicon particle with a 1 μm diameter deposited on the edges of the bottom substrates using a UV-curable polymer (HUV 8001 T, HNC Technology). The prepared top and bottom substrates were combined under UV exposure, resulting in a sandwich cell configuration. The MeOPh-BTBT-C8 powder was located at the entrance of the sandwich cell, and then it was heated to near the N to Iso phase transition temperature of MeOPh-BTBT-C8 (~275 °C) to fill the sandwich cell by capillary forces.

Optical characterization of LC structures in sandwich cells

Polarized optical microscopy (POM) (LV100POL, Nikon, Tokyo, Japan) was used to exhibit the optical textures of the MeOPh-BTBT-C8 films at different temperatures with a flipping process. The birefringence intensity of the orientation-controlled LC films within the sandwich cells, including the hybrid anchoring conditions, was quantitatively analyzed by UV–vis spectroscopy (SPECTRA max Plus 384, Molecular Devices, Sunnyvale, CA) with a light source at 540 nm with sample rotation.

Structural characterization at the molecular scale

Grazing incidence X-ray diffraction (GIXD) experiments were conducted with 9 A U-SAXS and 6D C&S UNIST-PAL beamlines at the Pohang Accelerator Laboratory (PAL). The energy of the focused beam was ~11.06 keV, and the sample-to-detector distance (SDD) was ~221.26 mm, measuring the molecular and layer orientation. The diffraction patterns were recorded with a 2D CCD camera (Rayonix SX165).

Electrical characterization of the OFETs

The transfer and output curves of the bottom-gate top-contact OFET devices based on the orientation-controlled LC-OSC were measured by a Keithley 4200A-SCS semiconductor parameter analyzer in a nitrogen-filled glovebox. The charge carrier mobility (μ) was calculated by the equation below at the saturation region in the transfer curves:

$$I_{DS} = (WC_i/2L)\mu(V_{GS} - V_{th})^2$$

where W and L are the width (500 μm) and length (50 μm) of the S/D channel, respectively. C_i is the capacitance per unit area of the gate insulator (~75 pF mm^{-2}), and V_{th} is the threshold voltage extracted from a linear fitting of $-\sqrt{I_{DS}}$ versus $V_{GS.}$

Results and discussion

Molecular orientation control of LC-OSC

To realize our strategy, a small-molecular-weight LC-OSC, 2-(4-methoxyphenyl)−7-octyl-benzothienobenzothiophene (MeOPh-BTBT-C8), was prepared as previously reported (Fig. 1a)[38]. The differential scanning calorimetry (DSC) result shows the phase transition from the isotropic (Iso) to N, SmA, SmE, and Cr phases upon cooling (Fig. 1b), in which the N phase is the key to obtaining a long-range ordered structure. It is well known that there are three kinds of surface anchoring conditions in sandwiched substrates, including planar–planar, homeotropic–homeotropic, and hybrid anchoring conditions. Here, we prepare a planar anchoring polyimide (PA-PI) spin-coated sandwich cell, in which one substrate is treated by the uniaxial mechanical rubbing method, and the other remains under degenerated planar anchoring conditions. To investigate the molecular reorientation process by the flipping process, four steps are carried out: (i) LC-OSC is injected between the sandwich cell at a temperature near Iso to the N phase transition by capillary action, and the heating stage is placed beneath the sandwich cell to generate the thermal gradient, which is essential to control the domain-growing direction. Upon cooling at a rate of 10 °C min^{-1}, a phase transition occurs from the top to the bottom substrate due to the temperature gradient. In particular, when the phase transitions from the SmA to the SmE phase, LC-OSC aligns following the top rubbing anchoring condition with little influence of the bottom due to the relatively low temperature of the top regime, initiating the phase transition from the N to the SmE phase[41–43]. (ii) After cooling down to the Cr phase, the LC-OSC is flipped, resulting in an upside-down configuration compared to the previous configuration. To reorient the LC-OSC depending on the top substrate's anchoring condition, the sample is heated to a temperature near the Iso phase. (iii) Once again, the thermal gradient of the system affects the molecular orientation when the phase transition occurs from the N to the SmE phase, where it starts from the top substrate, as in (i) step. (iv) Cooling the sandwich cell to the Cr phase temperature shows a few defects due to the top PA-PI without rubbing the anchoring condition, in which the defects can be removed by self-healing behavior after repeating step (i).

Molecular reorientation property within one side rubbed sandwich cell

The flipping process is sequentially investigated by polarized optical microscopy (POM) (Fig. 2), in which the five representative phases of MeOPh-BTBT-C8 are observed, as shown in Fig. 2i–iv, coinciding with Fig. 1i–iv (Fig. 1). First, the top PA-PI rubbed/bottom PA-PI unrubbed configuration is cooled from (i) the Iso phase to (ii) the Cr phase with a schematic image of the molecular structure (Fig. 2a). The N phase shows a typical uniaxial aligned single domain, whose molecular director follows the top substrate's rubbing direction (RD) (red arrows). This means that the LC domain can grow from the top to the bottom due to the temperature gradient, as expected. The SmA phase also exhibits a uniform and uniaxial single domain of the LC-OSC without typical fan-shaped textures. In the SmE phase, striped patterns appear perpendicular to the molecular director parallel to the rubbing direction, resulting from the close herringbone packing of LC-OSC molecules, whose alignment characteristics are preserved to form the Cr phase[38,39].

To reorient LC-OSCs under the opposite anchoring conditions above, the sandwiched cell is flipped to have the top PA-PI unrubbed/bottom PA-PI rubbed configuration and heated to (iii) the Iso phase. Following the cooling process, the corresponding phase transition shows the sequential change in POM images, in which the single domain collapses, generating the defects marked with red dot circles appearing in the N phase, and they remain in the SmA phase. The nonuniform textures remain even after the transition to the SmE and Cr phases. The origin of these two different kinds of textures is based on the sandwich cell configuration, where two factors are considered: (1) increase of the surface azimuthal anchoring energy by rubbing process;[44–46] (2) temperature gradient, which is relevant to initiating the phase transition at a specific position, here the top substrate. Considering the higher anchoring energy of the rubbed PA-PI than that of the pristine PA-PI and the initiation of the phase transition from the relatively low-temperature region, the reorientation of LC-OSCs is simply possible depending on the anchoring condition of the top substrate by the flipping process. That is, in the case of the top PA-PI unrubbed/bottom PA-PI rubbed configuration, defects are generated because the phase transitions from the top substrate, although the bottom substrate has a higher anchoring energy due to the rubbing process (blue arrows).

To induce the self-healing of defects or reorient the LC-OSCs, the second flipping process is performed as shown in Fig. 2b, c. The sample is flipped to show the top PA-PI rubbed/bottom PA-PI unrubbed configuration as the same as the initial condition (Fig. 2a). The cooling process from the Iso to the Cr phase makes defects disappear, and

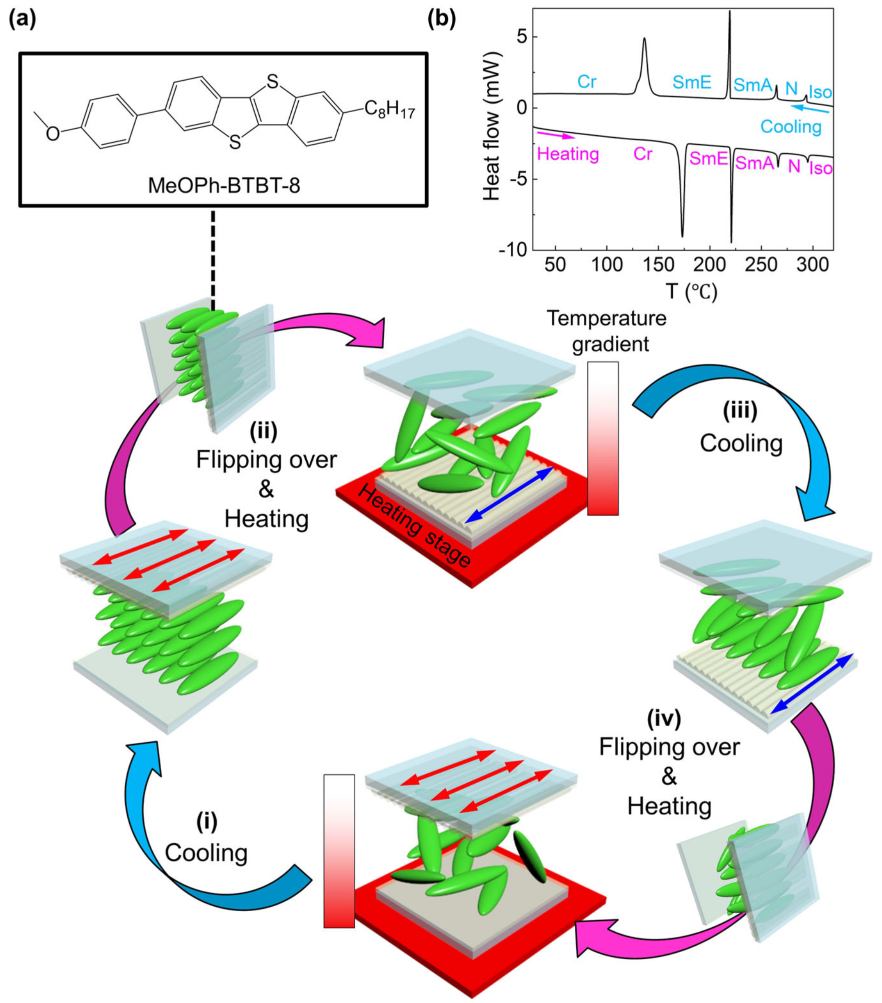

Fig. 1 Schematic illustration of the molecular orientation-controllable platform based on a liquid crystal organic semiconductor (LC-OSC) by flipping. a Chemical structure of MeOPh-BTBT-C8. **b** DSC curve obtained at 15 °C min^{-1}. (i–iv) Molecular reorientation process by flipping. (i) Uniaxially oriented LC-OSC in the sandwich cell in which one substrate is treated by the uniaxial mechanical rubbing method, and the other remains a degenerate planar anchoring condition. (ii) After the flipping process, the upside-down configuration of the sandwich cell undergoes heating, where the temperature of the top region is relatively lower than that of the bottom region. (iii) The cooling process causes nucleation and growth of the LC-OSC from the top region, in which few defects appear due to the top PA-PI without rubbing anchoring conditions. (iv) The defects can be removed by self-healing behavior after repeating step (i).

uniaxial orientation occurs along the RD (red arrows). Here, we can conclude that the N phase is critical for the orientation-controllable platform based on different rubbing and anchoring conditions.

Orthogonal molecular reorientation of LC-OSCs within orthogonally rubbed sandwich cells

In addition to the simple sandwich cell explained above, both side rubbed sandwich cells are demonstrated to show the versatility of our reorientation platform (Fig. 3). Previous results that have both side-uniaxially rubbed sandwich cells already showed highly oriented LC-OSCs along the RD[38]. To facilitate the solvent-free reorganization characteristics of the LC-OSC depending on the rubbing configuration related to the surface anchoring (Fig. 2), an orthogonally rubbed sandwich cell is employed, which is well known in twisted nematic (TN) cells in LC displays (LCDs). Following the cooling process after LC-OSC injection into the orthogonally rubbed sandwich cell, the molecular orientation is observed by POM with the schematic molecular configuration (Fig. 3a–h), in which the inset red and blue arrows indicate the top and bottom substrate RDs, respectively. The N phase (Fig. 3a) shows conventional TN arrangements, which reveal a bright domain while rotating the sample, although the intensity and birefringence color vary, which is induced by the twisted configuration of the molecules and the crossed polarizers. Even in the SmA phase,

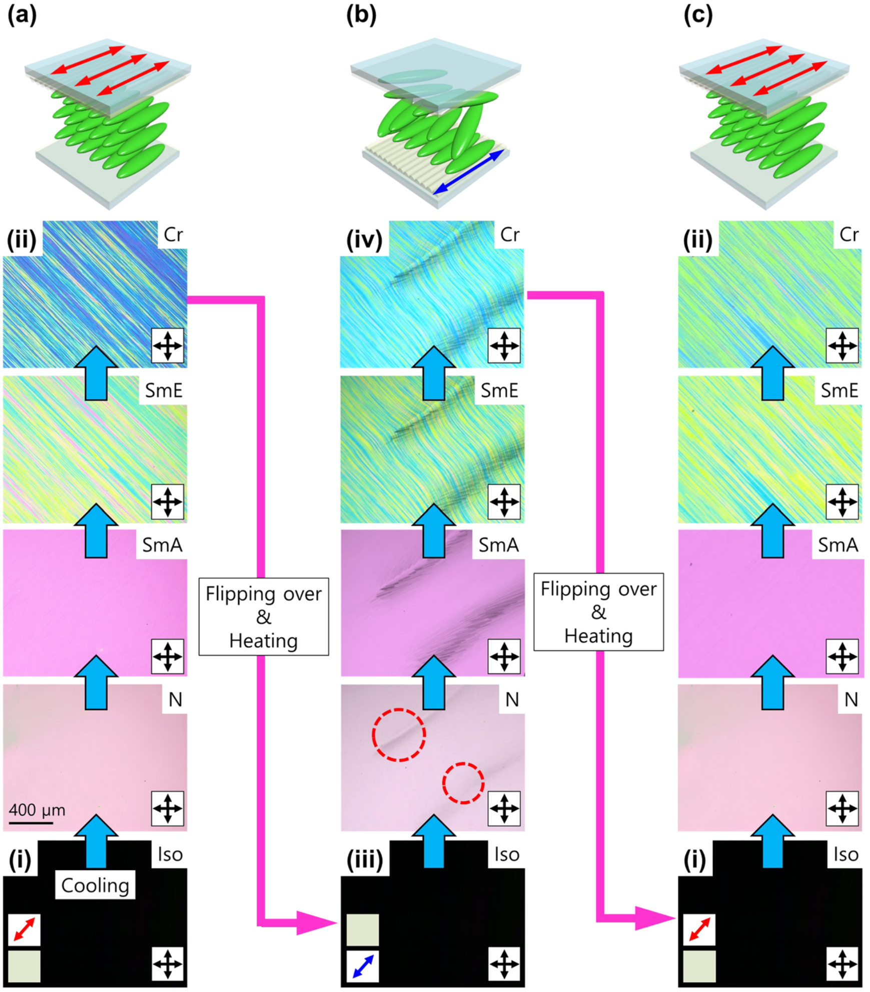

Fig. 2 Molecular reorientation process of one side rubbed sandwich cell measured by in situ polarized optical microscopy (POM). **a**, **b**, **c** Each schematic illustration of molecular orientation at the N phase following the flipping process within (**a**) the top PA-PI rubbed/bottom PA-PI unrubbed sandwich cell configuration. The orientation of the LC-OSC was measured by POM following the cooling process from the Iso to Cr phase. **b** After the flipping and heating processes, the upside-down platform generates different molecular orientations under the influence of the unrubbed top substrate condition, showing single-domain collapses with defects. **c** The second heating after the second flipping process makes the unaligned domains disappear under the influence of the rubbed top substrate condition.

relatively clear textures are observed, although some stain-like points appear (Fig. 3b). Due to the relatively higher elastic spring constant in the SmA phase than in the N phase, most molecular directors follow the top substrate's RD. When the RD of the top substrate is parallel to either the polarizer or the analyzer, the SmA domain exhibits a certain degree of extinction with the lined textures (inset of Fig. 3b), while it becomes bright when the RD is tilted to the polarizers. For the SmE phase, band-like textures with a long-band direction perpendicular to molecular directors are observed (Fig. 3c)[47]. The phase transition from N to SmE is subjective to the top substrate's surface anchoring and RD (red arrow). The POM results show dramatic birefringence changes when the sample is rotated, in which the SmE domain exhibits good extinction (inset of Fig. 3c). The schematic molecular arrangement at the SmE phase within the orthogonally rubbed sandwich cell is demonstrated in Fig. 3d. To reorient the LC-OSC with the upside-down configuration compared to the above configuration, the sample is flipped over and heated to the Iso phase temperature, in which the RD of the top and bottom substrates is now perpendicular to that of the former substrate. Following the same cooling process from the Iso to the SmE phase (Fig. 3e–g), the POM images show LC-OSCs oriented orthogonally compared to the previous configuration (Fig. 3a–c). Based on the positive birefringent MeOPh-BTBT-C8 molecule, blueish and yellowish domains appear when the optic axis is oriented parallel or perpendicular to the slow axis of the λ plate, respectively.

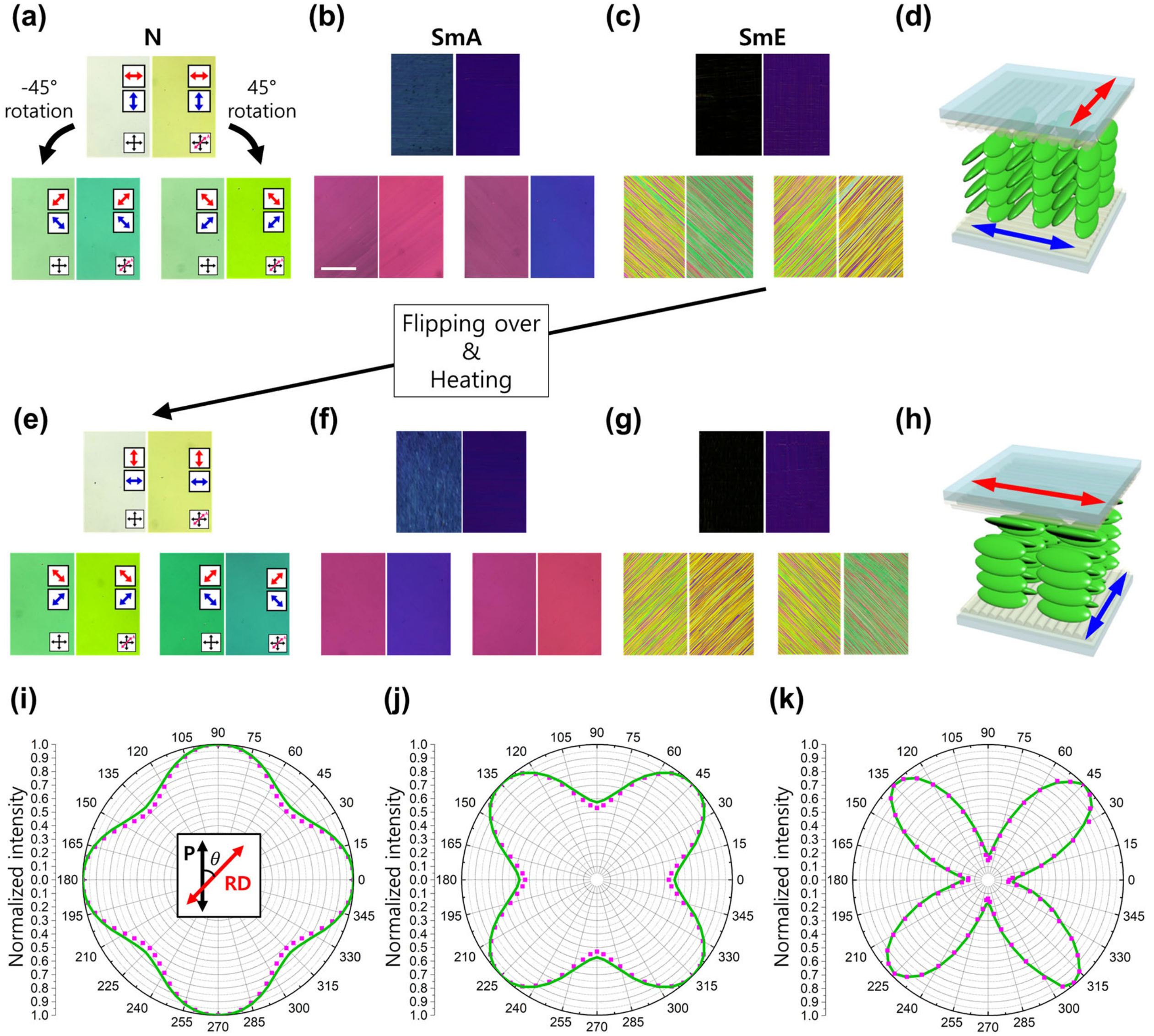

Fig. 3 Orthogonal molecular reorientation of an LC-OSC based on an orthogonally rubbed sandwich cell. a–c POM images of different phases (N, SmA, and SmE phases) with **d** schematic molecular orientation images of the SmE phase before and **e–h** after the flipping process. The scale bar within the POM result is 400 µm. Birefringence intensity profile as a function of rotation angle between the crossed polarizers before (red line) and after (blue line) the flipping process at the (**i**) N, (**j**) SmA, and (**k**) SmE phases.

By rotating the samples by ±45° under POM measurement with the λ plate, we can confirm that the LC-OSC molecules follow the top rubbing anchoring condition, and disclination lines are generated perpendicular to the top rubbing direction. The corresponding schematic molecular configuration of the SmE phase is demonstrated in Fig. 3h.

Additionally, a quantitative optical analysis is demonstrated as a function of the rotation angle (θ) between the RD of the top substrate and the polarizer in each LC phase (Fig. 3i–k). The green solid lines and pink dotted lines indicate the birefringent intensities before and after the flipping process, respectively. In the N phase, the highest transmittance appears at $\theta = 0$, 90, 180, and 270°. This can be explained by the phase shift of the incident light. In the TN domain, the light undergoes a phase shift of π/2 after passing through the cell, called the wave-guiding effect of LC[48]. Thus, the cell always exhibits the bright state under crossed polarizers; however, there is a slight decrease in the transmission at $\theta \neq 0$, 90, 180, and 270° due to the elliptically polarized light induced from LC molecules anchored on the rubbed PI films. The highest transmittance appears at $\theta = 0$, 90, 180, and 270° because the plane of the linearly polarized light passing through the TN LC domain is parallel to the optic axis of the analyzer. On the other hand, in the SmA and SmE phases (Fig. 3j and k), light transmission occurs when phase retardation is generated, as shown in Fig. 3b, c, f, and g[49]. Thus, a dark state appears when molecular directors are parallel or perpendicular to the polarizers ($\theta = 0$, 90, 180, 270°) due to the absence of phase retardation. Depending on the order parameter in the SmA and SmE phases with orthogonally rubbed sandwich cells, the degree of phase retardation or ordering is different, as shown in Fig. 3b, c, f, and g. The resultant transmittance intensities are summarized in Fig. 3j, k, in which the order parameter (S) of LC directors can be determined by the following equation[50,51],

$$S = (I_{\perp} - I_{\parallel})/(I_{\perp} + 2I_{\parallel})$$

where $I_{\perp}$ and $I_{\parallel}$ are the transmittance intensities when θ is 45 and 0°, respectively. The S-values of SmA and SmE are ~0.19 and 0.66, respectively.

Electrical characteristics of orientation-controllable LC-OSCs depending on the flipping process

To measure the electrical properties, we designed a bottom-gate top-contact (BGTC) OFET based on the Cr phase of MeOPh-BTBT-C8 in the sandwich cell (Fig. 4), consisting of PA-PI-coated indium tin oxide (ITO) glass substrates with a transistor channel width = 500 μm and length = 50 μm (Fig. 4a). The thickness and unit-area capacitance of the spin-coated PA-PI film are characterized in Supplementary Fig. S1. The RDs of the top and bottom substrates are orthogonal to control the molecular orientation by a flipping process. The charge carrier transport, a hole in this case, is believed to be governed by π–π interactions between the adjacent aromatic cores within the herringbone arrangement, in which the dominant π–π stacking direction is perpendicular to the RD[52]. This means that the holes transport along the long-band direction perpendicular to the molecular directors shown in the SmE phase (Fig. 3c, g). Initially, the RD condition of the sandwich cell is perpendicular and parallel to the source (S)/drain (D) channel direction of the top and bottom substrates, respectively. In the system, LC-OSCs are aligned with a uniaxial planar configuration guaranteeing three-dimensional (3D) electrical hole transport, which is comparable to 2D transport of vertical orientation fabricated by the solution-processed open-cell method under the strong homeotropic anchoring manner of air[25]. Following the cooling process to the Cr phase (Fig. 4b), it is confirmed that the π–π stacking direction is parallel to the S/D channel direction, inducing favorable hole transport. Here, the RDs of the top and bottom substrates are perpendicular and parallel to the S/D channel direction, respectively. To reorient the LC-OSC, the sandwich cell is flipped and undergoes heating to the Iso phase, followed by the cooling process to the Cr phase, which is shown in the middle of the POM image in Fig. 4b. Additionally, the sandwich cell is flipped, and the heating and cooling process is carried out, as shown in the right POM image of Fig. 4b. The π–π stacking direction is parallel to the S/D channel direction with a favorable hole transport configuration. The representative transfer and output characteristics are measured for each condition during the flipping process (Fig. 4c and Supplementary Fig. S2). All OFET measurements were conducted at room temperature, ~23 °C. In the graphs, black, blue, and red lines correspond to the initial, first flipped, and second flipped states, respectively. As a result, Fig. 4c shows the hole mobility for each RD of the top substrate during the flipping process with the corresponding on/off ratio (I_{ON}/I_{OFF}) and threshold voltage (V_{th}). The dotted and solid lines in Fig. 4c correspond to the forward and backward sweep currents, exhibiting negligible hysteresis.

Based on the sandwich cell system, it is difficult to demonstrate thermotropic LC-OSC patterning related to the vertical and lateral leakage currents. For the unpatterned OSC layer, current leaks from the source to the gate electrode via a wide OSC region due to the electric field between the source/drain gate, causing increased power consumption. Moreover, the generation of lateral leakage derived from the unpatterned OSC creates a lateral leakage path with a fringe current, inducing mobility overestimation[53,54]. These undesirable increases in the on-current with overestimated mobility result in an inaccurate operation of the devices, which are inherent problems to overcome in subsequent research to realize patterning of thermotropic LC-OSCs.

Following the first flipping state, the LC-OSC exhibits a parallel orientation to the source/drain channel direction from the perpendicular orientation at the initial state, resulting in a V_{th} shift toward negative values. Note that the molecular orientation direction is perpendicular to the π–π stacking direction, corresponding to a favorable charge transport direction. This can be derived from the more interfacial charge traps for the first flipping state due to the deep grain boundaries perpendicular to the channel conduction direction, which can deteriorate the charge transport[55,56]. For the second flipping state, the molecular direction is changed from parallel to perpendicular to the channel direction, which is the same molecular orientation as the initial state. The V_{th} shifted toward positive values is derived from the fewer interfacial charge traps. The hole mobility is calculated in the saturation region ($V_{SD} = -50$ V) of the transfer curves (Table 1), which is confirmed by the additional mobility graphs at a saturation region as a function of V_{GS} (Fig. 4d). Thus, the hole mobility from the orthogonal molecular orientation following the flipping exhibits an electrical anisotropy ratio ($\mu_{\perp}/\mu_{\parallel}$) of ~14.3.

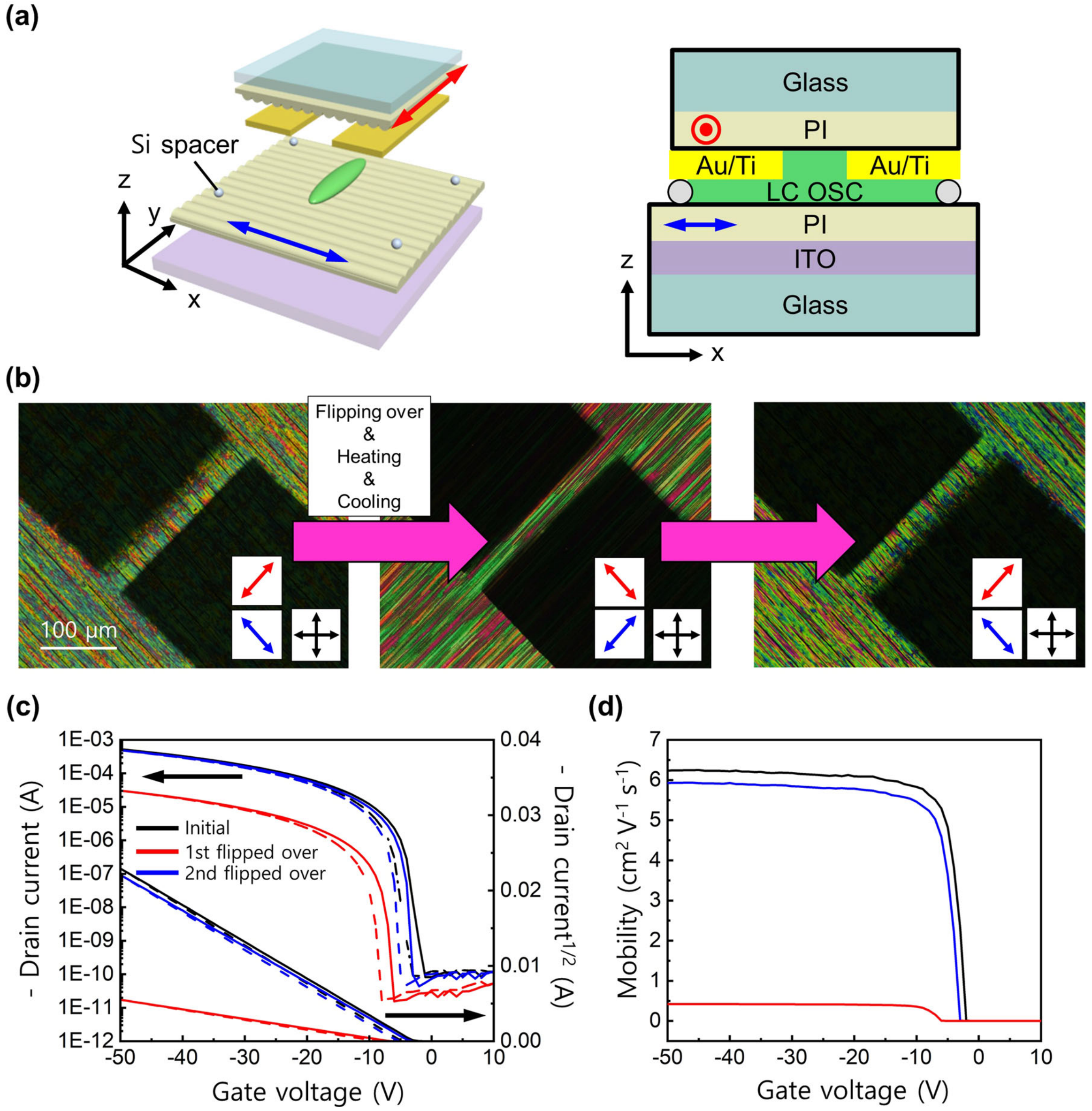

Fig. 4 Electrical characterization of orientation-controllable LC-OSC following the flipping process. a Bottom-gate bottom-contact OFET configuration based on a sandwich cell with a cross-section view exhibiting different anchoring and rubbing conditions of PI. **b** Sequential POM images of an orthogonally rubbed PI condition-based sandwich cell following the flipping process. **c** Transfer curves of OFETs of an orthogonal rubbed sandwich cell at $V_{DS} = -50$ V. **d** Mobility as a function of V_{GS} of OFETs following the flipping.

To nucleate and grow MeOPh-BTBT-C8 by facilitating thermotropic LC properties, time to raise and lower the temperature is needed for the phase transition from the isotropic to crystal phase. For the sandwich cell-based experimental conditions, the heating and cooling rate of the heating stage was 10 °C/min, in which it takes ~15 min for one overall phase transition corresponding to one electrical switching time, which is relatively short compared to the general post-thermal annealing process time (~1 h) of the OSC films. However, the challenges of electrical switching resulting from the high transition temperature from the LC phase to the isotropic phase can be solved by subsequent research, including adding a pendant group, although this can deteriorate the charge carrier mobility.

The modulation of molecular orientation and electrical behavior is tuned by different cooling rates, such as 10 °C/min and quenching from N to Cr temperature (Supplementary Fig. S3). Based on grazing-incidence X-ray diffraction (GIXD) analysis (Fig. S3a), the (*020*) diffraction peak distribution is compared, corresponding to π–π stacking within the herringbone configuration.

Table 1 Electrical characteristics of OFETs based on an orthogonally rubbed sandwich cell following the flipping process.

Sample	Mobility (cm^2 V^{-1} s^{-1})	I_{ON}/I_{OFF}	V_{th} (V)
Perpendicular (initial)	6.19 ± 2.02	~10^6	−(2.6 ± 1.8)
Parallel (1st flip)	0.43 ± 0.14	~10^5	−(6.8 ± 3.2)
Perpendicular (2nd flip)	6.16 ± 2.11	~10^6	−(3.2 ± 2.1)

The standard deviation was extracted from the data of ten devices.

Compared with the 10 °C/min condition, the quenched sample shows high ordering with face-on orientation with respect to the substrate by confirming a full-width half-maximum at $\chi \sim 90°$ and a distribution of 1D circular plot distribution (Supplementary Fig. S3b), although the POM texture difference is negligible (Supplementary Fig. S3c). Furthermore, the electrical behavior difference depending on the cooling rate is demonstrated (Supplementary Fig. S3d). Based on the highly ordered and oriented LC-OSC obtained by quenching at N temperature, the charge carrier mobility of the quenched LC-OSC is ~21.05 cm^{2}V^{-1}s^{-1}, which is 3.4 times higher than the result obtained at 10 °C/min.

Molecular orientation of LC-OSC within the different sandwich cell conditions

The crystalline structure and molecular orientation of MeOPh-BTBT-C8 samples were investigated by synchrotron powder X-ray diffraction (PXRD) and 2D-grazing incidence X-ray diffraction (2D-GIXD), respectively (Fig. 5). After obtaining the possible unit cell parameters and space group of the MeOPh-BTBT-C8 powder sample with EXPO software (Fig. 5a)[57], an orthorhombic crystal structure ($P2_12_12$ space group) with $a = 5.9605$ Å, $b = 7.7051$ Å, $c = 52.47$ Å, $\alpha = \beta = \gamma = 90°$ could be obtained using the profile matching (LeBail) method of FullProf suite (Fig. 5b and Supplementary Table S1)[58]. The thin-film samples for GIXD experiments were prepared by detaching the sandwich cells in the Cr phase, in which X-rays were incident in the direction parallel and perpendicular to the rubbing direction to obtain the molecular orientation. MeOPh-BTBT-C8 films based on rubbed PA-PI sandwich cells show well-aligned diffraction peaks, which indicate a typical herringbone molecular structure based on SmE-like polar ordering modulated parallel to the substrate with the face-on configuration and tilting ~22° from the long axis (Fig. 5b,c). However, within the vertical anchoring (VA)-PI-based sandwich cell (Fig. 5d), the molecular arrangement exhibits an edge-on configuration, whose optical texture is measured in each LC phase by POM (Supplementary Fig. S4). For the unrubbed PA-PI condition (Supplementary Fig. S5), the molecular arrangement exhibits both edge-on and tilted face-on configurations compared to the VA-PI case.

Due to the limitations of X-ray penetration depth under GIXD conditions[59], sample preparation has limitations for the top substrate detachment of the sandwich cell, resulting in challenges for temperature-dependent GIXD measurement. However, because the POM measurement visualizes the overall molecular orientation within the sandwich cell depending on the temperature change and the allowance of the quantitative birefringence intensity comparison, it supports molecular orientation switching following the flipping process.

Contact resistance of LC-OSC-based OFETs for different surface anchoring energies

In terms of the charge injection along with the metal/OSC interfaces in the BGTC-OFET configuration, the contact resistance (R_C) can be considered the critical parameter determining the charge carrier mobility. In particular, it has played an increasingly important role because the length of the channel has been reduced and the OFET operated under the low electric field[60,61]. Previous work has demonstrated a different energy level alignment of the metal/OSC interface depending on molecular orientation[62–64], in which the face-on molecular orientation has shown better energy band alignment between the Au-work function and OSC HOMO level, leading to lower contact resistance. For our system, the modulated molecular orientation depending on the surface anchoring energy of PI induces a different R_C. The R_C of each S/D electrode is calculated by the transfer-line method by varying the channel length (L) by 50, 100, 150, and 200 μm with a constant channel width of 500 μm (Supplementary Fig. S4) at $V_{GS} = -50$ V. The R_C is extracted from the $L = 0$ intersection of the resistances at each V_G, with the following equation:

$$R_{total} = R_C + \frac{L}{WC_i\mu_i}(V_G - V_{T,i}) = R_C + R_{ch}$$

where μ_i and $V_{T,i}$ are the intrinsic field-effect mobility and the threshold voltage, respectively. The calculated $R_{C\text{-values}}$ of VA-PI and PA-PI with parallel (||) and perpendicular (⊥) molecular orientations to the S/D channel direction are ~10.5, 1.58, and 1.21 kΩ cm, respectively (Supplementary Fig. S6). The additional transfer and output curves of OFET based on the VA-PI are shown in Supplementary Fig. 7.

Conclusions

We succeeded in modulating the long-range alignment and OFET properties using the LC characteristics of low-molecular-weight LC-OSCs. Here, the two most

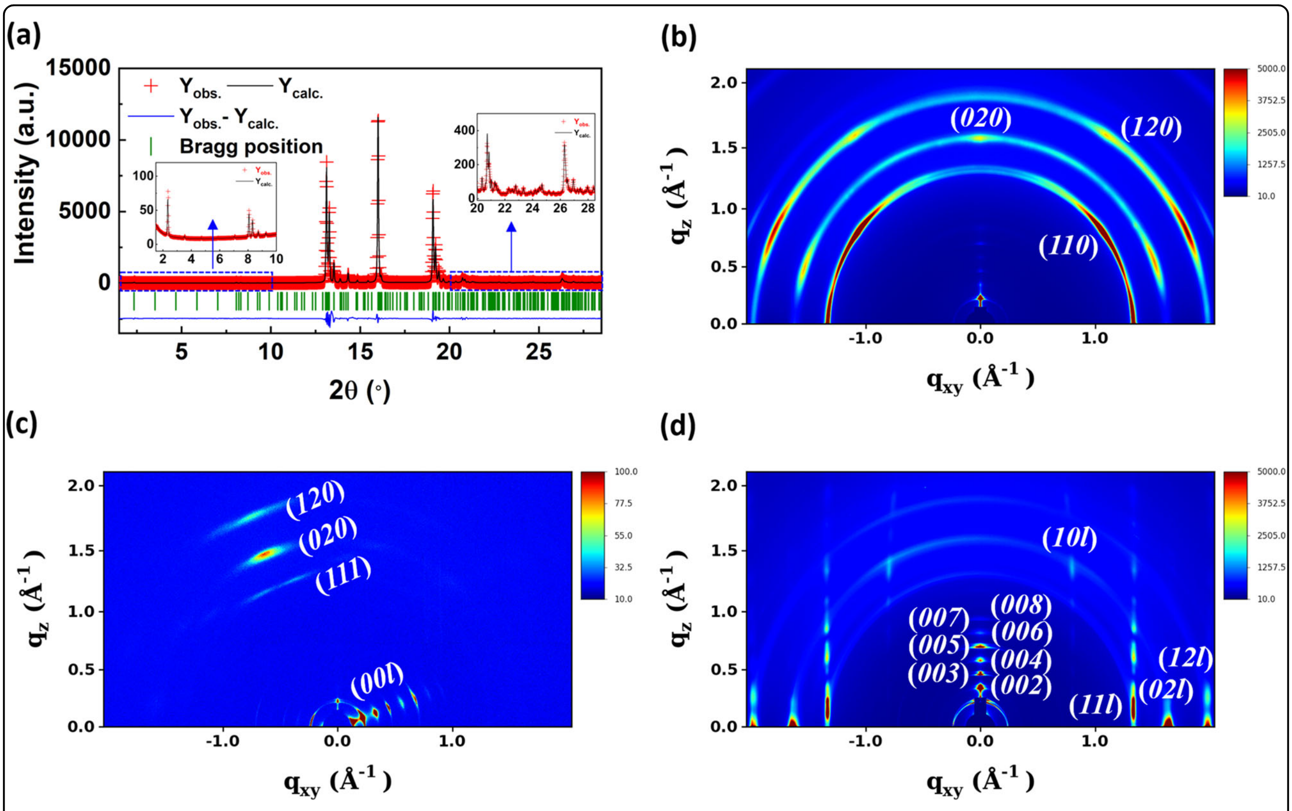

Fig. 5 PXRD and GIXD patterns of MeOPh-BTBT-C8 samples. a PXRD and whole pattern profile matching (LeBail method) results. For the rubbed PA-PI sandwich cell, the direction of the incident X-ray beam was (**b**) parallel and (**c**) perpendicular to the rubbing direction, in which the face-on orientation was oriented to the substrate. **d** In the VA-PI-based sandwich cell, the peaks indicated the mainly edge-on orientation to the substrate.

important parts in this work are the N phase that can enable the long-range arrangement of LC-OSCs and the temperature gradient in sandwich cells made of rubbed PA-PI substrates. By flipping the sandwich cell, the uniaxial orientation of the LC-OSC could be varied depending on the configuration of the sandwich cell on the heating stage. The well-aligned manner in the N phase is preserved even after transitioning to the solid-like SmE phase, guaranteeing a high charge carrier mobility in the Cr phase. Optically observed results on the modulated molecular orientations, with in situ monitoring by POM following the flipping process, are in good agreement with varied charge carrier mobilities measured by the OFETs. Our platform is a promising tool to control anisotropic organic electronic devices based on stimulus–response supramolecular semiconductors.

Acknowledgements

This was supported by a grant from the National Research Foundation (NRF) funded by the Korean Government (MSIT: 2017R1E1A1A01072798, 2021M3H4A3A01050378, 2018R1A5A1025224, 2019K1A3A1A21031284, and 2021R1A6A3A14039290). It was also supported by the Soft Materials Research Center under US NSF MRSEC Grant DMR-1420736. The experiments at the PLS-II were supported in part by MSIT and POSTECH.

Author details

[1]Graduate School of Nanoscience and Technology, Korea Advanced Institute of Science and Technology (KAIST), Daejeon 34141, Republic of Korea. [2]School of Materials Science and Engineering, Georgia Institute of Technology, Atlanta, GA 30332, USA. [3]Department of Chemistry, University of Colorado, Boulder, CO 80309, USA. [4]Department of Chemistry, Korea Advanced Institute of Science and Technology (KAIST), Daejeon 34141, Republic of Korea. [5]UNIST Central Research Facilities, Ulsan National Institute of Science and Technology (UNIST), Ulsan 44919, Republic of Korea. [6]Pohang Accelerator Laboratory, POSTECH, Pohang 37673, Republic of Korea. [7]Gradute School of Semiconductors and Devices Engineering, Ulsan National Institute of Science and Technology (UNIST), Ulsan 44919, Republic of Korea. [8]KAIST Institute for NanoCentury, Korea Advanced Institute of Science and Technology (KAIST), Daejeon 34141, Republic of Korea

Author contributions

M.J.H. and D.K.Y. designed the research; M.J.H. and H.S.Y. performed experimental works and D.W. and D.M.W. synthesized MeOPh-BTBT-C8 molecules; S.L, H.A., and T.J.S. helped with GIXD measurements and analyzed the molecular orientations; M.J.H., T.J.S., and D.K.Y. analyzed the results and wrote the manuscript.

Competing interests

The authors declare no competing interests.

Publisher's note

Supplementary information The online version contains supplementary material available at https://doi.org/10.1038/s41427-022-00377-5.

Received: 25 October 2021 Revised: 8 February 2022 Accepted: 25 February 2022.

References

1. Guo, Y., Yu, G. & Liu, Y. Functional organic field-effect transistors. *Adv. Mater.* **22**, 4427–4447 (2010).
2. Jeong, J. et al. Ultrasensitive detection of hazardous reactive oxygen species using flexible organic transistors with polyphenol-embedded conjugated polymer sensing layers. *J. Hazard Mater.* **355**, 17–24 (2018).
3. Lin, P. & Yan, F. Organic thin-film transistors for chemical and biological sensing. *Adv. Mater.* **24**, 34–51 (2012).
4. Torsi, L., Magliulo, M., Manoli, K. & Palazzo, G. Organic field-effect transistor sensors: a tutorial review. *Chem. Soc. Rev.* **42**, 8612 (2013).
5. Someya, T. & Sakurai, T. Integration of organic field-effect transistors and rubbery pressure sensors for artificial skin applications. *Tech. Dig.* 203−206 (2003).
6. Mushrush, M., Facchetti, A., Lefenfeld, M., Katz, H. E. & Marks, T. J. Easily processable phenylene−thiophene-based organic field-effect transistors and solution-fabricated nonvolatile transistor memory elements. *J. Am. Chem. Soc.* **125**, 9414–9423 (2003).
7. Heremans, P. et al. Polymer and organic nonvolatile memory devices. *Chem. Mater.* **23**, 341–358 (2011).
8. Di, C., Zhang, F. & Zhu, D. Multi-functional integration of organic field-effect transistors (OFETs): advances and perspectives. *Adv. Mater.* **25**, 313–330 (2013).
9. Templier, F., Aventurier, B., Demars, P., Botrel, J.-L. & Martin, P. Fabrication of high performance low temperature poly-silicon backplanes on metal foil for flexible active-matrix organic light emission diode displays. *Thin Solid Films* **515**, 7428–7432 (2007).
10. Mizukami, M. et al. Flexibleo organic light-emitting diode displays driven by inkjet-printed high-mobility organic thin-film transistors. *IEEE Electron Device Lett.* **39**, 39–42 (2018).
11. Lee, S., Jeon, S., Chaji, R. & Nathan, A. Transparent semiconducting oxide technology for touch free interactive flexible displays. *Proc. IEEE* **103**, 644–664 (2015).
12. Ling, M. M. & Bao, Z. Thin film deposition, patterning, and printing in organic thin film transistors. *Chem. Mater.* **16**, 4824–4840 (2004).
13. Chu, P.-H. et al. Toward precision control of nanofiber orientation in conjugated polymer thin films: impact on charge transport. *Chem. Mater.* **28**, 9099–9109 (2016).
14. Jimison, L. H., Toney, M. F., McCulloch, I., Heeney, M. & Salleo, A. Charge-transport anisotropy due to grain boundaries in directionally crystallized thin films of regioregular poly(3-hexylthiophene). *Adv. Mater.* **21**, 1568–1572 (2009).
15. Diao, Y. et al. Solution coating of large-area organic semiconductor thin films with aligned single-crystalline domains. *Nat. Mater.* **12**, 665–671 (2013).
16. Nakayama, K. et al. Patternable solution-crystallized organic transistors with high charge carrier mobility. *Adv. Mater.* **23**, 1626–1629 (2011).
17. Minemawari, H. et al. Inkjet printing of single-crystal films. *Nature* **475**, 364–367 (2011).
18. Goto, O. et al. Organic single-crystal arrays from solution-phase growth using micropattern with nucleation control region. *Adv. Mater.* **24**, 1117–1122 (2012).
19. Schweicher, G. et al. Bulky end-capped [1]benzothieno[3,2-*b*]benzothiophenes: reaching high-mobility organic semiconductors by fine tuning of the crystalline solid-state order. *Adv. Mater.* **27**, 3066–3072 (2015).
20. Diao, Y., Shaw, L., Bao, Z. & Mannsfeld, S. C. B. Morphology control strategies for solution-processed organic semiconductor thin films. *Energy Environ. Sci.* **7**, 2145–2159 (2014).
21. Qian, J. et al. Solution-processed 2D molecular crystals: fabrication techniques, transistor applications, and physics. *Adv. Mater. Technol.* **4**, 1800182 (2019).
22. Smith, J. et al. Solution-processed small molecule-polymer blend organic thin-film transistors with hole mobility greater than 5 cm^2/Vs. *Adv. Mater.* **24**, 2441–2446 (2012).
23. Kline, R. J. et al. Dependence of regioregular poly(3-hexylthiophene) film morphology and field-effect mobility on molecular weight. *Macromolecules* **38**, 3312–3319 (2005).
24. Janneck, R., Vercesi, F., Heremans, P., Genoe, J. & Rolin, C. Predictive model for the meniscus-guided coating of high-quality organic single-crystalline thin films. *Adv. Mater.* **28**, 8007–8013 (2016).
25. Yuan, Y. et al. Ultra-high mobility transparent organic thin film transistors grown by an off-centre spin-coating method. *Nat. Commun.* **5**, 3005 (2014).
26. Sirringhaus, H. et al. Two-dimensional charge transport in self-organized, high-mobility conjugated polymers. *Nature* **401**, 685–688 (1999).
27. McCulloch, I. et al. Liquid-crystalline semiconducting polymers with high charge-carrier mobility. *Nat. Mater.* **5**, 328–333 (2006).
28. Li, M.-H., Keller, P., Yang, J. & Albouy, P.-A. An artificial muscle with lamellar structure based on a nematic triblock copolymer. *Adv. Mater.* **16**, 1922–1925 (2004).
29. Ahir, S. V., Tajbakhsh, A. R. & Terentjev, E. M. Self-assembled shape-memory fibers of triblock liquid-crystal polymers. *Adv. Funct. Mater.* **16**, 556–560 (2006).
30. Kumar, M., Gowda, A. & Kumar, S. Discotic liquid crystals with graphene: supramolecular self-assembly to applications. *Part. Part. Syst. Charact.* **34**, 1700003 (2017).
31. Heilmeier, G. H. & Zanoni, L. Guest-host interactions in nematic liquid crystals. A new electro-optic effect. *Appl. Phys. Lett.* **13**, 91–92 (1968).
32. Choi, Y., Choi, T.-H., Woo, J.-H., Jeon, B.-G. & Yoon, T.-H. Fast turn-off switching of vertically-aligned negative liquid crystals by fine patterning of pixel electrodes. *Crystals* **7**, 201 (2017).
33. Park, W. et al. Directed self-assembly of a helical nanofilament liquid crystal phase for use as structural color reflectors. *NPG Asia Mater.* **11**, 45 (2019).
34. Kim, D. S., Lee, W., Lopez-Leon, T. & Yoon, D. K. Self-regulated smectic emulsion with switchable lasing application. *Small* **15**, 1903818 (2019).
35. Kim, D. S., Cha, Y. J., Kim, M. H., Lavrentovich, O. D. & Yoon, D. K. Controlling Gaussian and mean curvatures at microscale by sublimation and condensation of smectic liquid crystals. *Nat. Commun.* **7**, 10236 (2016).
36. Hoogboom, J., Rasing, T., Rowan, A. E. & Nolte, R. J. M. LCD alignment layers. Controlling nematic domain properties. *J. Mater. Chem.* **16**, 1305–1314 (2006).
37. Ryu, S. H. et al. Creation of liquid-crystal periodic zigzags by surface treatment and thermal annealing. *Soft Matter* **11**, 8584–8589 (2015).
38. Han, M. J. et al. Highly oriented liquid crystal semiconductor for organic field-effect transistors. *ACS Cent. Sci.* **4**, 1495–1502 (2018).
39. Iino, H., Usui, T. & Hanna, J. Liquid crystals for organic thin-film transistors. *Nat. Commun.* **6**, 6828 (2015).
40. Wu, H., Iino, H. & Hanna, J. Thermally induced bilayered crystals in a solution-processed polycrystalline thin film of phenylterthiophene-based monoalkyl smectic liquid crystals and their effect on FET mobility. *RSC Adv.* **7**, 56586–56593 (2017).
41. Kim, H. et al. Multistep hierarchical self-assembly of chiral nanopore arrays. *Proc. Natl. Acad. Sci. USA* **111**, 14342–14347 (2014).
42. Lee, S. et al. Physico-chemical confinement of helical nanofilaments. *Soft Matter* **11**, 3653–3659 (2015).
43. Lee, S. et al. Multidimensional helical nanostructures in multiscale nanochannels. *Langmuir* **31**, 8156–8161 (2015).
44. Jo, S. I., Kim, Y., Baek, J.-H., Yu, C.-J. & Kim, J.-H. Highly polarized emission of the liquid crystalline conjugated polymer by controlling the surface anchoring energy. *Jpn. J. Appl. Phys.* **53**, 03CD04 (2014).
45. Gerus, I., Glushchenko, A., Kwon, S.-B., Reshetnyak, V. & Reznikov, Y. Anchoring of a liquid crystal on a photoaligning layer with varying surface morphology. *Liq. Cryst.* **28**, 1709–1713 (2001).
46. Andrienko, D., Dyadyusha, A., Iljin, A., Kurioz, Y. U. & Reznikov, Y. U. Measurement of azimuthal anchoring energy of nematic liquid crystal on photoaligning polymer surface. *Mol. Cryst. Liq. Cryst.* **321**, 271–281 (1998).
47. Kim, D. S., Cha, Y. J., Gim, M.-J. & Yoon, D. K. Fast fabrication of sub-200-nm nanogrooves using liquid crystal material. *ACS Appl. Mater. Interfaces* **8**, 11851–11856 (2016).
48. Kim, J., Kim, D., Yu, C. & Lee, S. A new transflective geometry of low twisted nematic liquid crystal display having a single cell gap. *J. Inf. Disp.* **5**, 14–17 (2004).
49. Choi, B., Song, S., Jeong, S. M., Chung, S.-H. & Glushchenko, A. Electrically tunable birefringence of a polymer composite with long-range orientational ordering of liquid crystals. *Opt. Express* **22**, 18027 (2014).
50. Tokuhisa, H., Era, M. & Tsutsui, T. Polarized electroluminescence from smectic mesophase. *Appl. Phys. Lett.* **72**, 2639–2641 (1998).
51. Joo, S.-H., Kim, J.-K. & Song, J.-K. Fluorescent light source with continuously tunable polarization via modification of molecular orientation. *J. Appl. Phys.* **114**, 083508 (2013).

52. Izawa, T., Miyazaki, E. & Takimiya, K. Molecular ordering of high-performance soluble molecular semiconductors and re-evaluation of their field-effect transistor characteristics. *Adv. Mater.* **20**, 3388–3392 (2008).
53. Chen, C. et al. Thin-film transistors with the fringe effect and the correction factor for mobility extraction. *IEEE Electron Device Lett.* **40**, 897–900 (2019).
54. Park, J., Zhang, X., Bae, M.-H., Park, G.-T. & Bae, J.-H. Fringe field effect on electrical characteristics of pentacene thin-film transistors. *Jpn. J. Appl. Phys.* **52**, 111602 (2013).
55. Haneef, H. F., Zeidell, A. M. & Jurchescu, O. D. Charge carrier traps in organic semiconductors: a review on the underlying physics and impact on electronic devices. *J. Mater. Chem. C.* **8**, 759–787 (2020).
56. Tello, M., Chiesa, M., Duffy, C. M. & Sirringhaus, H. Charge trapping in intergrain regions of pentacene thin film transistors. *Adv. Funct. Mater.* **18**, 3907–3913 (2008).
57. Altomare, A. et al. EXPO2013: A kit of tools for phasing crystal structures from powder data. *J. Appl. Cryst.* **46**, 1231–1235 (2013).
58. Rodríguez-Carvajal, J. Recent advances in magnetic structure determination by neutron powder diffraction. *Phys. B* **192**, 55–69 (1993).
59. Saito, I. et al. Orientation and relaxation behaviors of lamellar microdomains of poly(methyl methacrylate)-b-poly(n-butyl acrylate) thin films as revealed by grazing-incidence small-angle X-ray scattering. *Polym. J.* **48**, 399–406 (2016).
60. Liu, C., Xu, Y. & Noh, Y.-Y. Contact engineering in organic field-effect transistors. *Mater. Today* **18**, 79–96 (2015).
61. Khaliq, A., Xue, F. L. & Varahramyan, K. Numerical simulation of spin coated P3HT organic thin film transistors with field dependent mobility and distributed contact resistance. *Microelectron. Eng.* **86**, 2312–2315 (2009).
62. Gargi, D. et al. Charge transport in highly face-on poly(3-hexylthiophene) films. *J. Phys. Chem. C.* **117**, 17421–17428 (2013).
63. Lee, W. H. et al. Surface-directed molecular assembly of pentacene on monolayer graphene for high-performance organic transistors. *J. Am. Chem. Soc.* **133**, 4447–4454 (2011).
64. Fabiano, S., Yoshida, H., Chen, Z., Facchetti, A. & Loi, M. A. Orientation-dependent electronic structures and charge transport mechanisms in ultrathin polymeric n-channel field-effect transistors. *ACS Appl. Mater. Interfaces* **5**, 4417–4422 (2013).